MMIC Vector Topology Enabling Multi RF Functionalities for 5G and Beyond

Christophe Loyez, Michael Bocquet, Kamel Haddadi

MMIC Vector Topology Enabling Multi RF Functionalities for 5G and Beyond

**CHRISTOPHE LOYEZ, (Member, IEEE), MICHAEL BOCQUET,
AND KAMEL HADDADI [ID], (Member, IEEE)**

Univ. Lille, CNRS, Centrale Lille, Univ. Polytechnique Hauts-de-France, UMR 8520 - IEMN - Institut d'Electronique de Microélectronique et de Nanotechnologie, F-59000 Lille, France
Centre National de la Recherche Scientifique, Université Lille, USR 3380 - IRCICA, Lille, France

Corresponding author: Kamel Haddadi (kamel.haddadi@univ-lille.fr)

ABSTRACT This paper presents a vector topology of a monolithic microwave integrated circuit (MMIC) capable of performing several radiofrequency (RF) functionalities essential for future wireless communications and geolocation in the millimeter frequency band. The proposed circuit can address several usage modes such as conventional frequency heterodyning for high-speed IQ modulation and demodulation. In addition, the device can be configured in six-port quadratic detection mode to achieve optimum power added efficiency (PAE). The topology developed in 65 nm FDSOI CMOS technology achieves broadband V-band frequency operation and combines vector precision for both high data rates and phase state determination. The results presented concern QPSK modulation schemes at data rates up to 4 Gbps as well as essential geolocation metrics such as time domain of arrival (TDoA) and angle of arrival (AoA). The combination of vector accuracy/PAE together with wide linear operating range makes this topology a viable candidate for next generation radio frequency systems.

INDEX TERMS Monolithic microwave integrated circuit (MMIC), IQ modulation/demodulation, millimeter wave, six-port technology, time domain of arrival (TDoA), angle of arrival (AoA).

I. INTRODUCTION

A tremendous amount of 5G and 6G future applications rely on microwave or millimeter (mm-wave) wave systems [1]. This market will continue to drive the increase of the utilized frequency spectrum as well as the required bandwidth [2]–[4]. Common and well-established approaches for microwave and mm-wave systems are mostly based on active circuitry today, like heterodyne or homodyne architectures [5], [6]. The benefits of using active microwave systems are good sensitivity and dynamic range combined with good miniaturization capabilities. However, all these active stages require power for their operation and several auxiliary stages with limited power efficiency (PAE). The PAE becomes a critical factor in future systems, aiming at high frequency and high data rate. Active circuitry requires energy for its operation, so PAE cannot be the maximum if auxiliary stages must be used. This fact will cause severe energy resource problems, concerning the envisioned wireless and

digitalization trend for using millions or even billions of such systems in the future and expanding the operating frequency range as well as bandwidth.

There is an urgent need to adapt radio frequency (RF) devices and circuits to these new usages. In particular, future wireless systems need to provide multiple functionalities to minimize the overall footprint and energy balance [2], [7]–[9]. Moreover, the use of higher frequencies, particularly in the millimeter-wave frequency range, has been confirmed through successive generations of radio communication networks.

In this context a quasi-passive approach comes into play: The Six-Port architecture [10]. Initially developed for microwave network analysis, this approach has been addressed to generic direct-conversion system, receiver as well as transmitter in 1994 [11], [12].The six-port technology utilizes only a few active components, e.g., a sinusoidal local oscillator and a low noise or power amplifier [13]–[17]. No additional active stages are required. This pushes the PAE to the maximum and simply outperforms commonly used active circuitry concerning energy efficiency. Although the

Six-Port's drawbacks, i.e., low sensitivity and dynamic range, limit the penetration of related applications in the microwave frequency range, the Six-Port approach will be extremely beneficial for future systems, especially for applications in the mm-wave frequency range [18]–[25].

The authors have contributed to the dissemination of the Six-Port technology for microwave and mm-wave vector network analysis [26]–[30], telecommunications and localization [31]–[33], short-range radars [34], [35] and electromagnetic sensing [36], [37]. Based on our previous works, the authors propose a fully integrated V-band architecture to provide both localization and modulation/demodulation functionalities. Each of these functionalities has already been demonstrated at the scale of a monolithic integration with high performance and level of integration [38]–[42]. The motivation of this study is to highlight the possibility of realizing all these functionalities from the same stand-alone MMIC topology which could be involved in a more complete system. The main idea is to combine advantages of both heterodyne and six-port technologies that can operate as a function of available millimeter-wave power. In Section II, the design of the proposed Millimeter-wave Monolithic Integrated Circuit (MMIC) is presented in detail by decomposing the overall behavior into two distinct modes based respectively on heterodyne frequency mixing and six-port detection. Section III demonstrates the intrinsic performance in terms of bandwidth, vector accuracy and energy efficiency. Experimental performances in V-band are then presented with emphasis on the linear operating range and the wideband behavior of the modulation and demodulation functions of the vector topology. In Section IV, the detection and extraction functions of the TDoA and AoA metrics required for geolocation at 60 GHz are described. The fusion of these AoA/TDoA metrics as well as the performances are demonstrated.

II. DESIGN OF THE MMIC FOR MULTI RF FUNCTIONALITIES

In this section, we introduce the topology which is the object of the study aiming at demonstrating the possibility of realizing the functionalities of modulation/demodulation on the one hand and quadratic detection of localization specific metrics on the other hand. Indeed, CMOS technology has made it possible to reach millimeter frequencies for several years: these offer the advantage of being able to integrate radio frequency and digital functions on the same chip. The energy consumption is limited by the low supply voltage of around one volt, which makes it possible to reach emission powers of up to several tens of milliWatts: this order of magnitude makes them compatible with several applications. A new generation of RF front-end can provide several functionalities on the same chip. Among the candidates allowing this plurality, direct conversion architectures seem to stand out in particular. Indeed, their ability to operate in the vector domain gives them an additional degree of freedom allowing them to pool several functionalities within the same MMIC.
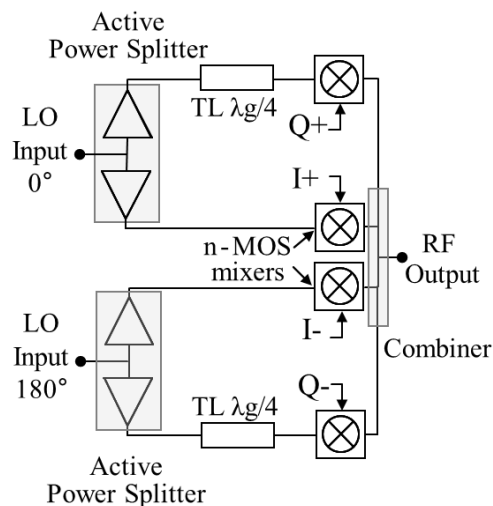

FIGURE 1. Synoptic of the overall MMIC topology (modulation configuration).

A. GLOBAL TOPOLOGY

In this sub-section, we focus on the overall architecture: Fig. 1 describes this overall architecture based on the topology of a direct-conversion IQ modulator/demodulator, both up and down frequency conversion. The design requires overcoming several limitations related to the fact that the different local oscillator (LO) and RF microwave inputs both operate in the same millimeter wave range. It is therefore essential to be able to contain the cross-talks between the different channels. This is made possible in particular by the play of phase shifts as described below. From a global point of view, this architecture includes one differential LO input, one RF port configurable in input or output mode, and four baseband ports corresponding to the differential in-phase I^+, I^- and quadrature Q^+, Q^- signals. By adjusting the phase shifts, the leakage of the signal provided by the local oscillator (LO signal) is cancelled and the baseband I and Q channels are balanced. For this purpose, this vector topology of MMIC is illustrated in Fig. 1. The phase shifts, provided by differential LO inputs together with quarter-wavelength $\lambda_g/4$ transmission lines (TL), are induced on the four different baseband ports are 0°, 90°, 180° and 270° respectively. The differential signal of the 60 GHz LO is distributed over the four baseband channels using two active power splitters. These provide the necessary isolation (>25 dB) between the different baseband channels and amplify the signals distributed in this way.

B. ACTIVE PHASE SHIFTER

This subsection is devoted to the power dividers whose role in the overall topology is described in Figure 1 and whose design is critical to the global operation. Fig. 2(a) shows the electrical diagram of the active power splitters. Each of these active power dividers consists of two 50 Ohm cascode stages matched at the input and output. The matching network is designed in coplanar technology (CPW) to ensure matching and maximum gain. Each cascode stage consists
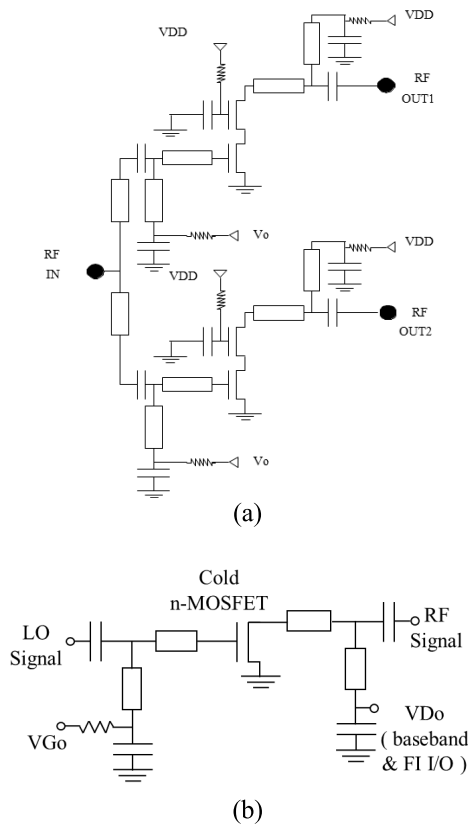
FIGURE 2. (a) Electrical schematic of the active power splitter. (b) Electrical schematic of the n-MOS mixer.

of two transistors with 50 μm gate width a 60 nm gate length with 40 gate fingers. The common source transistors are biased by an external voltage $V_0 = 0.6$ V on the gate via high value poly-silicon resistors. The bias of the common gate transistors is connected to the supply voltage V_{DD} ($V_1 = 1.2$ V) to get maximum gain. The RF decoupling between the stages and the RF shunts at the end of the line are realized with metal-oxide-metal (MOM) capacitors. In particular, capacitance values of 1.5 pF and 25×25 μm^2 are used. The power gain of the cascode amplifier is equal to 5.5 dB with a 1 dB output compression point (OCP1-dB) of 6 dBm. At the 60 GHz frequency value, the simulated characteristics of the power splitter are the following: the isolation between each of the two outputs and the input is equal to 25dB (19.5 dB between the two outputs). The transmission parameters are equal to 2.3 dB between the input and the outputs while the reflection coefficients are respectively equal to -9.1 dB for the splitter input and -17dB for the outputs. The inverse isolation of 25 dB is a crucial parameter that prevents the dialogue between the four different ways.

C. PHASE SHIFTER AND MIXER

After having described the power divider, we are interested in mixers and phase shifters whose vocation is to allow to operate in the vector domain. A phase-shifter is associated to

each power splitter in order to generate replicas of the LO signal with quadrature phase-shifts. The equal distribution of the input power to the output ports guarantees the amplitude balance between them. The design of the phase shifter determines the accurate phase balance between the I and Q differential channels (subsequently referred to as I^+, I^- and Q^+, Q^- signals.)

The $-90°$ phase shift is performed at 60 GHz using an additional transmission delay line. In concrete terms, this phase-shift deviates from $-90°$ only slightly around the center frequency. Then four mixers operate four frequency beats in parallel. These frequency beats result in an upward or downward frequency conversion, depending on whether the MMIC operates as a modulator or demodulator respectively. Each mixer involves an n-MOSFET whose gate only is biased to minimize conversion losses. As described in Fig. 2(b), the source is connected to ground and the drain to the 50 Ohm RF port decoupled by a capacitor, thus preserving the DC power consumption that is zero at rest.

III. OPERATING MODES

At this stage of the description, two very distinct operating modes should be considered. The first one is the heterodyne mode for which the modulation/demodulation functionalities are examined. The second mode is the quadratic mode which is directly involved in the extraction of AoA and TDoA.

A. HETERODYNE MODE

The first mode corresponds to the case where the order of power of the LO signal power is close to the milliwatt. This mode corresponds to the conventional heterodyne architecture to address IQ modulation and demodulation functions. In this case, each mixer is simultaneously pumped by each of the phase-shifted contributions of the LO signal and can be considered, as a first approximation, as a switch in the ON or OFF state. This hashing in the time domain induces the frequency transposition of the desired incident signal. This frequency transposition can be up-conversion or down-conversion. By adjustments of the phase-shifts, when I^+, I^- and Q^+, Q^- signals are configured as input signals (at V_D access), the MMIC allows to realize the functionality of a vector modulator. Therefore, the equation of the output signal RF(t) can be expressed as follows:

$$RF(t) = k_I \cdot \left(I^+(t) - I^-(t) \right) \cdot \left(\cos(\omega_{LO} \cdot t + \theta_{LO}) \right. $$
$$\left. - k_Q \cdot \left(Q^+(t) - Q^-(t) \right) \cdot (\sin(\omega_{LO} \cdot t + \theta_{LO}) \right. \quad (1)$$

In the case of down-conversion, the RF(t) signal is configured as an input signal and the I^+, I^- and Q^+, Q^- signals then correspond to output signals. After digital filtering applied off-line after sampling the signals. These signals thus result from a convolution (*) with the impulse response $h_{BF}(t)$ of these digital Low Pass (LP) filters. Typically, these one correspond to root-raised cosine filters with roll-coefficient coefficients $\alpha = 0.35$. By this way, the expressions of these differential output signals (at V_D access) are expressed as

follows:

$$I^+(t) = h_{LP}(t) * [k_{I+}.RF(t).(\cos(\omega_{LO}.t + \theta'_{LO}))] \quad (2)$$

$$I^-(t) = h_{LP}(t) * [k_{I-}.RF(t).(-\cos(\omega_{LO}.t + \theta'_{LO}))] \quad (3)$$

$$Q^+(t) = h_{LP}(t) * [k_{Q+}.RF(t).(\sin(\omega_{LO}.t + \theta'_{LO}))] \quad (4)$$

$$Q^-(t) = h_{LP}(t) * [k_{Q-}.RF(t).(-\sin(\omega_{LO}.t + \theta'_{LO}))] \quad (5)$$

In both cases, the optimal power required for the LO signal is −2 dBm.

B. QUADRATIC DETECTION MODE AND RELATED SIX-PORT TOPOLOGY

The second regime corresponds to the case of quadratic detection where the incident signals, LO and RF, both have a microwave power not exceeding −20 dBm. Each phase-shifted contribution of the LO signal is incident at one end of one of the four passive mixers. The other ends of the mixer receive a portion of the other RF signal. The signals are then combined directly within the common source n-MOSFET without the need for an additional power splitter or coupler, thus avoiding an increase in overall space requirements.

As mentioned Fig 2. (b), V_{Do} and V_{Go} correspond respectively to the Drain voltage and the Gate voltage at rest. The V_{DG} voltage ($V_{DG} = V_{Do} - V_{Go}$), measured in DC operation when RF and LO signals are applied, then corresponds to the quadratic sensing voltage. Considering the respective expressions for the signals LO and RF, the detected voltage can be expressed as follows:

$$s_{LO}(t) = A_{LO}e^{j(\omega_{LO}t + \varphi_{LO})}$$

$$s_{RF}(t) = A_{RF}e^{j(\omega_{RF}t + \varphi_{RF})}$$

$$\begin{aligned} V_{DG} &= \gamma |s_{LO}(t) - s_{RF}(t)|^2 \\ &= \gamma \left(A_{LO}^2 + A_{RF}^2 - A_{LO}.A_{RF}.\cos[(\omega_{RF}t + \varphi_{RF}) \right. \\ &\left. - (\omega_{LO}t + \varphi_{LO})] \right) \end{aligned} \quad (6)$$

The factor γ quantifies the sensitivity of each n-MOS mixer. For each of the four contributions I^+, I^- and Q^+, Q^-, the first of the two terms in relation (6) are rectified signals, while the last contains, in sinusoidal form, the signal of interest (amplitude and phase–shift).

IV. TIME DIFFERENCE OF ARRIVAL AND ANGLE OF ARRIVAL ESTIMATIONS

We consider a configuration for which this vector topology allows the detection of both the Time Difference of Arrival (TDoA) and the Angle of Arrival (AoA) by quadratic detection. As described in Fig. 3, the global system topology involving the MMIC mainly comprises two patch antennas followed by two low noise amplifiers. The power gain and the noise figure are respectively equal to 42 dB and 6 dB. The LO (differential) and RF (single-ended) signals received and amplified are collected by the MMIC.

An essential parameter is the distance d between the antennas that need to be set to the free-space half-wavelength ($\lambda/2$) for AoA measurement. This distance requires to be of several
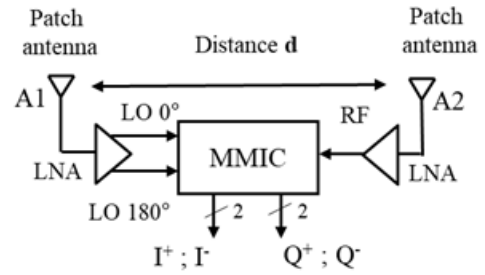

FIGURE 3. AoA/TDoA configuration involving the V-band vector MMIC.

free-space wavelengths for TDoA and closely depend on the RF signal bandwidth. As a function of the distance d between the antennas A1 and A2 and the waveform signal emitted by the transmitter, the vector topology described above can estimate the AoA as well as the TDoA. When d = $\lambda/2$, the phase difference $\Delta\varphi = \pi.\sin(\text{AoA})$ can be extracted from the differential I(t) and Q(t) signals. Typically, these signals are expressed as follows:

$$I^+(t) = k_1(A_{LO}^2 + A_{RF}^2 - 2A_{LO}A_{RF}\cos\Delta\varphi) \quad (7)$$

$$Q^+(t) = k_2(A_{LO}^2 + A_{RF}^2 + 2A_{LO}A_{RF}\sin\Delta\varphi) \quad (8)$$

$$I^-(t) = k_3(A_{LO}^2 + A_{RF}^2 + 2A_{LO}A_{RF}\cos\Delta\varphi) \quad (9)$$

$$Q^-(t) = k_4(A_{LO}^2 + A_{RF}^2 - 2A_{LO}A_{RF}\sin\Delta\varphi) \quad (10)$$

To optimize the TDOA measurement, the distance d is set to c/BW where BW is the bandwidth of the overall system. In this condition, the TDOA can be extracted from the envelope of the signal m(t) where:

$$m(t)^2 = I^+(t).I^-(t)^* + Q^+(t).Q^-(t)^* \quad (11)$$

For the experimental set-up, we have considered a frequency bandwidth BW equal to 3 GHz resulting in a distance d = 2c/BW, i.e. 5 cm to optimize TDoA extraction. The I+, I− and Q+, Q− signals are acquired in parallel by a 4-channel Keysight® scope with a sampling frequency of 10 GSa/s. The acquisition technique is based on triggered records of these four signals. The recording time is set to 500 ns resulting in a number of samples equal to 50,000 per waveform that are processed offline to determine the envelop m(t) by using Equation (11). For several RF source positions, TDoA values are then extracted from m(t) by an autocorrelation algorithm.

V. RESULTS AND DISCUSSION

A. INTRINSIC PERFORMANCE

Concerning the tests, we first examine the performance of the heterodyning mode by considering unmodulated sinusoidal signals at the input: the LO inputs and the RF output at 60 GHz are respectively applied and collected on the MMIC using on-wafer probes operating in V-band. The MMIC, whose micrograph is presented in Fig. 4, is first tested by considering the Single Side Band (SSB) mixer mode.

The experimental setup includes a power signal generator (Agilent® E8257D PSG), a spectrum analyzer
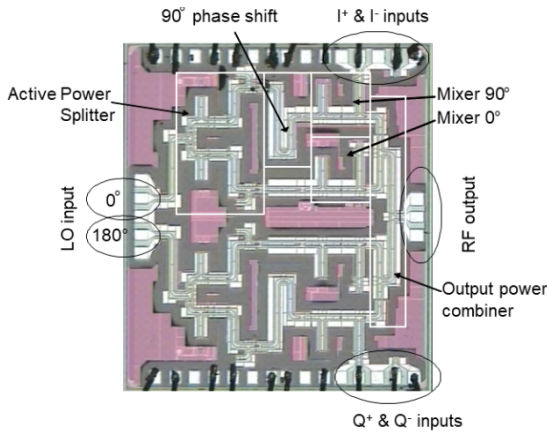
FIGURE 4. Micrograph of the overall MMIC topology (modulation configuration).

(a)

(b)

FIGURE 5. (a) Experimental SSB performance versus input LO frequency. (b) Experimental SSB performance versus input intermediate frequency.

(Rohde & Schwarz® FSU67) and an arbitrary waveform generator (Tektronix® AWG 7102). In order to evaluate the intrinsic SSB performance, the test bench is configured to measure the image frequency rejection, which makes it possible to rule on the quality of the equilibrium in both phase-shift and sustained amplitude between the different channels. For this purpose, the arbitrary waveform generator provides four synchronous sinusoidal signals with a phase shift of 0°, 90°, 180° and 270° respectively.

Fig. 5(a) and 5(b) show the measured conversion loss, image frequency rejection and LO-RF isolation as a function of the LO frequency. The frequency of the IF signal is set to 500 MHz in this case. In the frequency range from 57 GHz to 66 GHz, the average conversion loss is 10 dB with a ripple of less than 1 dB. These conversion losses are typical of a topology involving cold transistors for the frequency mixing which cannot produce any conversion gain. The LO to RF isolations range from 31 dB to 43 dB. Image frequency rejection is between 18 dB and 27 dB: this order of magnitude can only be obtained if the balance between channels is ensured both in amplitude and phase-shift since this parameter depends directly on these balances, regardless of the type of active or passive topology. This experimental result thus testifies to the expected vector behavior. Fig. 5 illustrates the RF operating bandwidth; in particular, the frequency response seen from the input for a LO frequency of 60 GHz. This shows that the 3 dB bandwidth is close to 1.25 GHz as seen from the input, while the image frequency rejection always remains above 15 dB over this range. Consequently, it can be concluded that the RF 3dB fractional bandwidth is 2.5 GHz at the 60 GHz center frequency which is suitable for modulations with a data rate greater than 1 Gigabit/s.

It is important to consider the low power used by the LO signal (-2dBm) to achieve these results. Also, the power of the RF modulated signal is measured at the output of the chip using a V-Band bolometer. Fig. 6 describes the evolution of the power of the RF signal at the output of the MMIC as a function of the input power. In this configuration of polarization of each of the four MOSFETs involved in
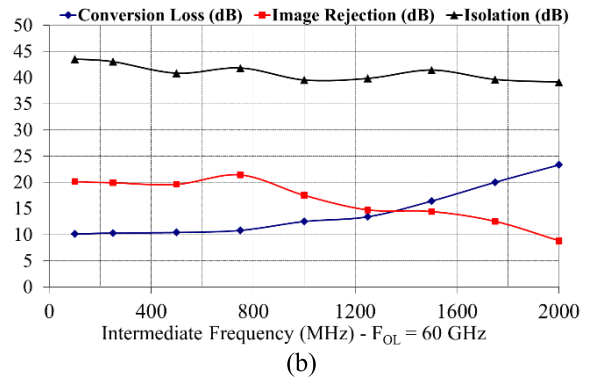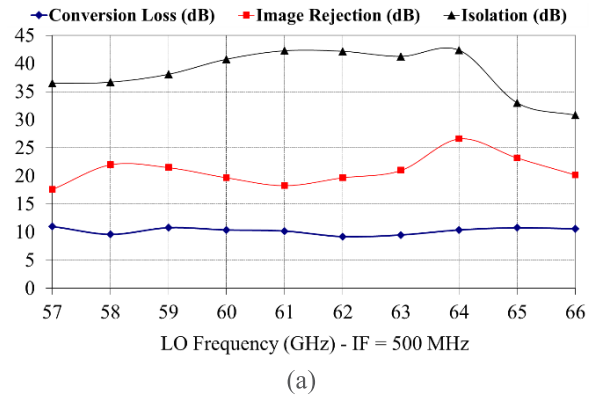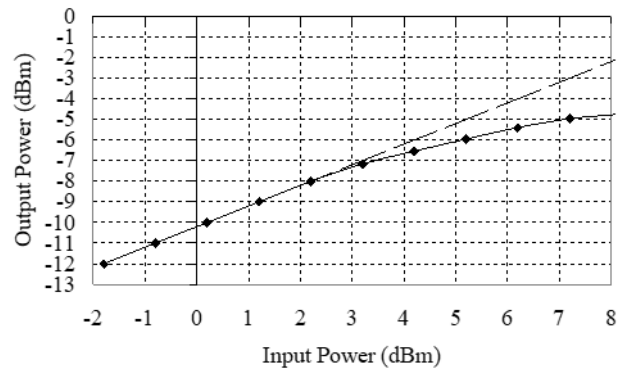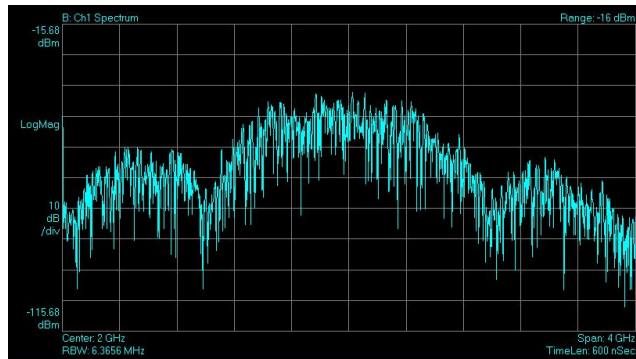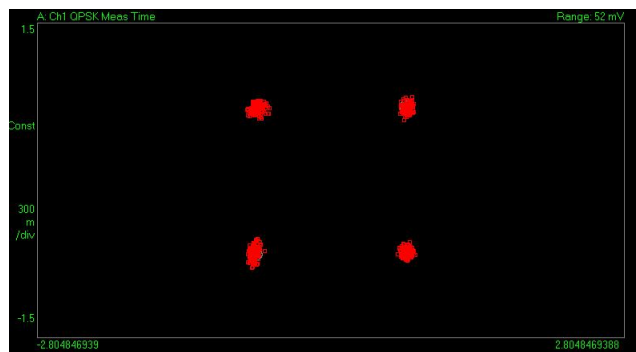

FIGURE 6. Measured RF output power (61 GHz) versus input IF power (0.5 GHz).

the frequency mixing, a high 1dB output compression point (1dBOCP) is obtained with respect to the absence of consumption of the transistor. The excellent linear behavior of the MMIC is highlighted. Indeed, its 1dBOCP is equal to -6 dBm at 61 GHz while its power consumption is only 24 mW. The value of this parameter 1dBOCP is sufficiently high not to penalize the overall emission chain. This means that the energy efficiency is 6 pJ/bit when the data rate reaches 4 Gbps.

FIGURE 7. (a) Measured power spectrum of the modulated signal. (b) Measured constellation diagram of the modulated signal after down-conversion. (QPSK – 1 Gbps – FLO = 60.5 GHz).

TABLE 1. EVM values (%) for a QPSK modulated signal at the MMIC RF output (PRF = Pout 1dBc).

Data rate	500 Mbps	1 Gbps	2 Gbps	3 Gbps	4 Gbps
Simulation	1.2 %	1.8 %	2.15 %	2.7 %	3.2%
Experiment	3.5 %	4.8 %	6.6 %	7.8 %	9.7 %

B. HETERODYNE MODE PERFORMANCE

In the first part of this section, we are interested in the heterodyne functionality in the context of vector modulation. This MMIC functionality is tested by considering a high throughput QPSK modulation scheme. The modulation signals are injected at the I+, I− and Q+, Q− inputs at rates of several Gigabits per second. In order to be able to quantify the vector accuracy of this operation, the RF signal resulting from this vector modulation is frequency down-converted using an external mixer. This RF signal is then converted into an intermediate frequency signal (IF = 1.5 GHz) which is then sampled using a fast digitizing scope. The power spectrum of the modulated signal is shown in Fig. 7(a). The vector accuracy of the modulation performed by the MMIC is then evaluated using vector signal analysis software. The constellation diagram of the analyzed signal is shown in Fig. 7(b). Table 1 summarizes the extracted error vector magnitude (EVM) measured for the QPSK modulation scheme for increasing data rates up to 4 Gbps.

TABLE 2. EVM values (%) for a QPSK demodulated signal.

Data rate	500 Mbps	1 Gbps	2 Gbps	3 Gbps	4 Gbps
Simulation	0.9 %	1.1 %	1.5 %	1.7 %	2.2%

It can be noted that these results are obtained under severe conditions since the power of the output RF signal has been chosen equal to the compression point at 1dB ($P_{RF} = P_{out}$ 1DBc = −6 dBm) to collect these measurements. Another point is the comparison between experimental results and simulation results from the modeling of the MMIC based on ADS Circuit Envelope simulation. We note a satisfactory concordance between our behavioral model and the experimental validation. It is estimated that the sources of divergence are mainly due to the test bench: in particular, the influence of the external mixer also induces degradations through its own non-linearities. Above all, the cables used limit the bandwidth of the test bench and degrade the quality of the signal when the data rates increase due to the higher spectral occupancy with respect to the cut-off frequency of these cables. The phase-shift/amplitude balance of the different channels announced by the SSB measurements is confirmed by these new results: since the EVM is less than 10% in this configuration, these experimental results validate the MMIC's vector modulation functionality. One can judge the excellent combination of precision/ power offered by this topology.

In the following, we focus the study on the vector demodulation or IQ demodulation functionality of the MMIC. For this configuration, we are limited by the test bench which requires a reference modulator to deliver a high-speed V-band modulated signal free of imperfections. This reference modulator is essential to be able to isolate the imperfections inherent to the MMIC configured as an IQ demodulator. The MMIC itself has attractive modulation performances for radio communications but these seem insufficient for metrology, especially since our test bench does not allow the cable de-embedding. We therefore rely on the behavioral model based on the Circuit Envelope ADS simulations whose results have been confirmed by the experimental results in the case of the MMIC configured as an IQ modulator. The performances predicted by this model are listed in Table 2.

As can be predicted theoretically, the simulation results are similar to the case of modulation with relatively weak vector errors. These results therefore presage a reciprocal behavior of the modulation/demodulation functionalities for this MMIC.

C. QUADRATIC DETECTION MODE

In order to evaluate the MMIC operating in quadratic detection, the measurement bench comprising two frequency generators (Keysight® E8257D PSG) used to generate LO and RF millimeter wave signals is modified. These generators are slaved on the same 10 MHz reference signal. The signals thus delivered are therefore frequency-synchronous.
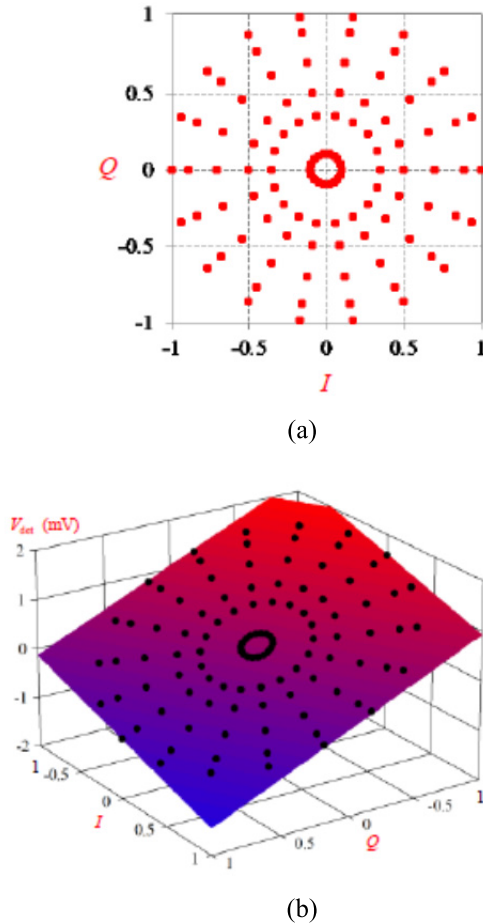
(a)

(b)

FIGURE 8. IQ quadratic detection at 60 GHz. (a) Constellation of the IQ reference symbols. (b) 3-dimensional fitting of the detected voltage Vdet as a function of I and Q; F = 60 GHz. (● Measured voltages).

In addition, the phase-shift and attenuation between the two waveforms are perfectly controlled. The measurement frequency is 60 GHz and the power at the input of the MMIC varies between −24 dBm and −19 dBm for the LO signal and between −44 dBm and −24 dBm for the RF signal.

For each combination of phase-shift and power, the detected voltages V_{det} relative to channels I^+, I^- and Q^+, Q^- are recorded. Phase -shift steps of $10°$ are considered in the range $0° – 360°$. The average error is calculated from the measured V_{det} voltages in each case. In the above-mentioned RF power range, the mean error is determined for LO power values below −20 dBm. The resulting I and Q reference data are depicted in Fig. 8. In this case, the mean error is determined experimentally to be in the order of 1.3%. Considering the compactness (die size: 1.54×1.77 mm^2) and power consumption (24 mW), this error obtained without any calibration validates the functionality of detecting the vector state of an incident RF signal in the context of an embedded system.

Under these conditions, we measure a relatively constant sensitivity for all frequencies between 50 GHz and 70 GHz. Typically, this sensitivity is of the order of 1.6 mV/μW
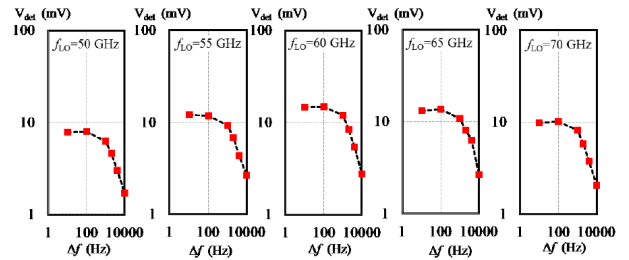

FIGURE 9. Measured video bandwidth vs. RF frequency: voltage detected as a function of frequency difference fRF - fLO.
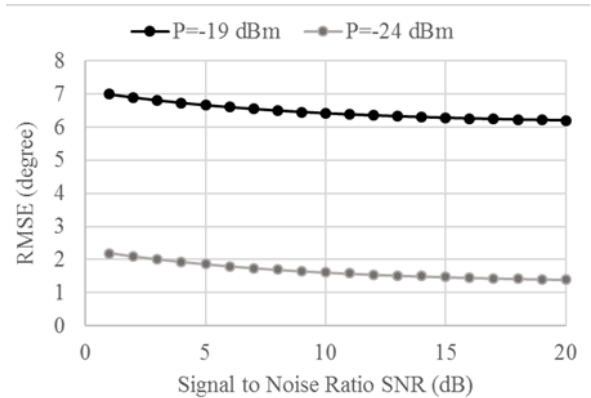

FIGURE 10. AoA root mean square error at the test frequency 61 GHz.

at 60 GHz while the mixers are not polarized (zero-bias). Also, the video bandwidth is evaluated by varying the frequency difference f_{RF} - f_{LO} between the two millimeter wave input signals up to 10 KHz. The experiments are performed between 50 and 70 GHz. The resulting data are shown in Fig. 9. Sensitivity and video bandwidth being competitive parameters, the resulting video bandwidth, measured at a 3 dB fractional bandwidth, is of the order of 4 KHz at 60 GHz. The center frequency does not significantly affect the measured sensitivity and video bandwidth.

D. TDoA/AoA DETERMINATION BASED ON QUADRATIC DETECTION MODE

As announced in Section IV, the combination of the detected voltages is used to estimate the angle of attack when the incoming RF signal is picked up by the receiver described by Fig. 3. Then, the root mean square error (RMSE) associated with the AOA estimate depends on both the received signal power and the noise level. From the behavioral model based on Circuit Envelope simulations, the evolution of the RMSE is established in Fig. 10 as a function of the signal-to-noise ratio (SNR) for received power values of −19 dBm and −24 dBm at the inputs of the MMIC. For a receive power equal to −24 dBm, the AoA RMSE remains around 2 degrees even under unfavorable SNR conditions. This highlights the robustness of the topology to thermal noise.
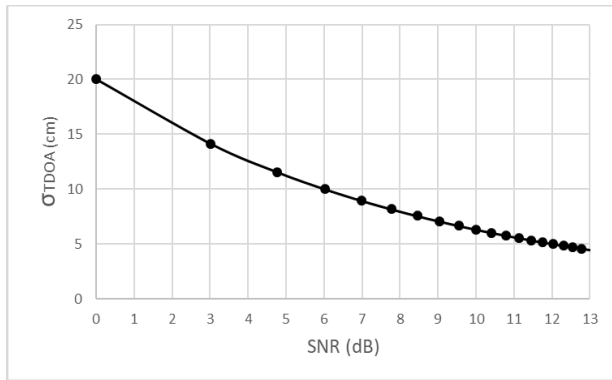
FIGURE 11. TDOA RMSE as a function of SNR – Fs = 10 GSa/s.

When the power is higher (−19 dBm), while the quadratic detection regime is less proven, the degradation remains contained since the AoA remains at an RMSE value less than or equal to 7 degrees. Note that this value is obtained without any calibration operation, which remains possible and is often used in six-port topologies.

This model thus allows to establish a link between the AoA accuracy and the received power as well as the SNR. In the same way, the accuracy of TDOA is evaluated. The sensitivity of the MMIC does not induce any significant degradation on the TDOA measurement. The sources of errors are mainly caused by the acquisition method (digitizing scope) and the extraction method (autocorrelation). With this operating mode, time resolution and RMSE are strongly dependent on the sampling frequency Indeed, the spatial RMSE related to the TDOA is expressed by:

$$\sigma_{TDOA} = \frac{2.c}{f_s.\sqrt{SNR}} \quad (12)$$

Based on this expression, Fig. 11 shows the evolution of the spatial RMSE (expressed in centimeters) as a function of the SNR for a sampling rate of 10 GSa/s. Typically the inaccuracy of the estimated TDOA is reflected in the distance domain by a deviation between 5 and 20 centimeters. This order of magnitude of the TDoA RSME is compatible with most applications. Nevertheless, this performance must be moderated by the use of a very high frequency sampler (10 GSamples per second) whose high cost may be a brake on the development of this TDoA-based solution.

Based on previous measurements and simulations, a model of the MMIC characteristics is built on Matlab, integrating its frequency and non-linear imperfections in the vector domain. On the basis of this model, a configuration of receivers integrating this MMIC is considered to detect both TDoA and AoA. As previously mentioned, the distance between antennas is a crucial parameter. In the case of TDoA, this distance is fixed at 5 cm while the value of 3 mm (λ/2) is used for the estimation of the AoA. Fig. 12 compares the performances of two locating systems: one comprises two synchronous receivers operating only in TDoA mode and the other consists of a single receiver allowing to combine the two
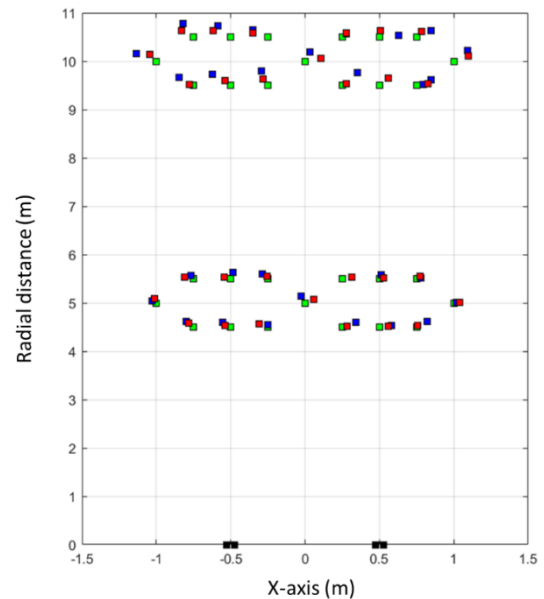

FIGURE 12. Estimated locations for the TDOA/TDOA combination (2 receivers spaced 1.2 m apart on the x-axis) and for the TDoA/AoA combination of a single receiver integrating the MMIC. Red dots: TDoA/AoA data fusion; Blue dots: TDoA/TDoA data fusion; Green dots: actual positions (dimensions are expressed in meters).

TABLE 3. Performance comparison table.

	[38]	[39]	[40]	[41]	[42]	This work
Technology	45nm SOI	65nm CMOS	45nm SOI	65nm CMOS	40 nm CMOS	65 nm CMOS
Frequency [GHz]	1-32	60	DC-60	3-5	60 GHz	57-66 GHz
Size (mm²)	NC	2 x 3	1 x 1.4	N.C.	1.1	1.54 x 1.77
Integration Level	Transmitter	Full transmitter	Modulator	Full transmitter	Full transmitter	Modulator /Demodulator
Data Rate (Gbps)	26	42	200	-	-	4
Heterodyne & Quadratic modes	No	No	No	No	No	yes
AoA error	-	-	-	1.5°	-	7° rmse
ToA/TDoA error	-	-	-	-	2.7 mm*	5 cm*
OP1dB [dBm]	18 (Psat)	6.5	-10	NC	NC	-6
PDC [mW]	490	151	200	NC	129	24

*High Signal to Noise conditions

modes and to merge TDoA/AoA. In order to validate the performance by a statistical approach, we considered more than hundred positions with radial distances of up to 10 meters in an intramural environment. The average error obtained is 28 centimeters in the case of TDoA versus 16 centimeters when considering the TDoA/AoA data fusion, which fully meets the specifications generally adopted for indoor geolocation systems.

E. PERFORMANCE COMPARISON

In order to assess the performance, we propose a comparison table to compare the performance of different MMICs from recent works.

This table shows that previous work has already highlighted the possibility of realizing the modulator or localization features through topologies specific to these features. The obtained performances are often superior to those proposed by this work. Nevertheless, none of these topologies allows us to assume a genericity of the usage modes (heterodyning and quadratic mode) or a versability on the functionalities in question.

Let us note that the topology proposes a size of MMIC and a competitive power consumption allowing a future degree of integration at the scale of a complete system integrating a local oscillator and power amplifier in the case of transmitters or low noise amplifiers in the case of receivers.

VI. CONCLUSION

It is now likely that the next generation of radio-frequency systems will incorporate artificial intelligence (AI), enabling them to better adapt to the constraints of their immediate environment. The flexibility of RF front-ends appears to be a prime candidate to allow this AI to develop. In this paper, the authors have proposed a versatile topology of MMIC. Although each functionality has already been demonstrated by the scientific community at the scale of an MMIC with superior performances in terms of bandwidth or accuracy, this work shows the possibility of realizing these functionalities on the basis of a single topology offering flexibility on heterodyne and quadratic detection modes. Through this work, the performances obtained show that it is possible to achieve several radiofrequency functionalities as modulation/demodulation as well as AoA/TDoA based localization in V-band on the basis of the same heterodyne/six-port chip. These results altogether demonstrate that the solution proposed is a viable and relevant contribution to this deployment perspective.

REFERENCES

[1] A. Ghosh, A. Maeder, M. Baker, and D. Chandramouli, "5G evolution: A view on 5G cellular technology beyond 3GPP release 15," IEEE Access, vol. 7, pp. 127639–127651, 2019, doi: 10.1109/ACCESS.2019.2939938.

[2] A. N. Uwaechia and N. M. Mahyuddin, "A comprehensive survey on millimeter wave communications for fifth-generation wireless networks: Feasibility and challenges," IEEE Access, vol. 8, pp. 62367–62414, 2020, doi: 10.1109/ACCESS.2020.2984204.

[3] Q. Jia, H. Xu, M. F. Xiong, B. Zhang, and J. Duan, "Omnidirectional solid angle beam-switching flexible array antenna in millimeter wave for 5G micro base station applications," IEEE Access, vol. 7, pp. 157027–157036, 2019, doi: 10.1109/ACCESS.2019.2946372.

[4] X. Cui, T. A. Gulliver, H. Song, and J. Li, "Real-time positioning based on millimeter wave device to device communications," IEEE Access, vol. 4, pp. 5520–5530, 2016, doi: 10.1109/ACCESS.2016.2604360.

[5] Y. Morishita, T. Teraoka, Y. Kashino, H. Asano, T. Sakamoto, N. Shirakata, K. Takinami, and K. Takahashi, "300-GHz-band self-heterodyne wireless system for real-time video transmission toward 6G," in Proc. IEEE Int. Symp. Radio-Freq. Integr. Technol. (RFIT), Sep. 2020, pp. 151–153, doi: 10.1109/RFIT49453.2020.9226182.

[6] S. Mondal, R. Singh, A. I. Hussein, and J. Paramesh, "A 25–30 GHz fully-connected hybrid beamforming receiver for MIMO communication," IEEE J. Solid-State Circuits, vol. 53, no. 5, pp. 1275–1287, May 2018, doi: 10.1109/JSSC.2018.2789402.

[7] A. Tahat, G. Kaddoum, S. Yousefi, S. Valaee, and F. Gagnon, "A look at the recent wireless positioning techniques with a focus on algorithms for moving receivers," IEEE Access, vol. 4, pp. 6652–6680, 2017, doi: 10.1109/ACCESS.2016.2606486.

[8] R. Zhang, J. Zhou, J. Lan, B. Yang, and Z. Yu, "A high-precision hybrid analog and digital beamforming transceiver system for 5G millimeter-wave communication," IEEE Access, vol. 7, pp. 83012–83023, 2019, doi: 10.1109/ACCESS.2019.2923836.

[9] X. Cui, T. A. Gulliver, J. Li, and H. Zhang, "Vehicle positioning using 5G millimeter-wave systems," IEEE Access, vol. 4, pp. 6964–6973, 2016, doi: 10.1109/ACCESS.2016.2615425.

[10] G. F. Engen, "The six-port reflectometer: An alternative network analyzer," IEEE Trans. Microw. Theory Techn., vol. MTT-25, no. 12, pp. 1075–1080, Dec. 1977, doi: 10.1109/TMTT.1977.1129277.

[11] J. Li, R. G. Bosisio, and K. Wu, "A six-port direct digital millimeter wave receiver," in Proc. IEEE Nat. Telesyst. Conf. (NTC), May 1994, pp. 79–82, doi: 10.1109/NTC.1994.316688.

[12] J. Li, R. G. Bosisio, and K. Wu, "Performing PSK demodulation using six-ports," in Proc. Symp. Antenna Technol. Appl. Electromagn. (ANTEM), Ottawa, ON, Canada, Aug. 1994, pp. 15–18.

[13] Y. Zhao, J.-F. Frigon, K. Wu, and R. G. Bosisio, "Multi(six)-port impulse radio for ultra-wideband," IEEE Trans. Microw. Theory Techn., vol. 54, no. 4, pp. 1707–1712, Jun. 2006, doi: 10.1109/TMTT.2006.871988.

[14] J. Östh, A. Serban, M. Karlsson, S. Gong, J. Haartsen, and P. Karlsson, "Six-port gigabit demodulator," IEEE Trans. Microw. Theory Techn., vol. 59, no. 1, pp. 125–131, Jan. 2011, doi: 10.1109/TMTT.2010.2091198.

[15] W. Zhang, A. Hasan, F. M. Ghannouchi, M. Helaoui, Y. Wu, and Y. Liu, "Concurrent dual-band receiver based on novel six-port correlator for wireless applications," IEEE Access, vol. 5, pp. 25826–25834, 2017, doi: 10.1109/ACCESS.2017.2768364.

[16] J. Östh, A. Serban, M. Karlsson, S. Gong, J. Haartsen, and P. Karlsson, "Six-port gigabit demodulator," IEEE Trans. Microw. Theory Techn., vol. 59, no. 1, pp. 125–131, Jan. 2011, doi: 10.1109/TMTT.2010.2091198.

[17] J. Li, R. G. Bosisio, and K. Wu, "Computer and measurement simulation of a new digital receiver operating directly at millimeter-wave frequencies," IEEE Trans. Microw. Theory Techn., vol. 43, no. 12, pp. 2766–2772, Dec. 1995, doi: 10.1109/22.475633.

[18] F. Lurz, F. Michler, B. Scheiner, R. Weigel, and A. Koelpin, "Microw(h)att?! ultralow-power six-port radar: Realizing highly integrated portable radar systems with good motion sensitivity at relatively low cost," IEEE Microw. Mag., vol. 19, no. 1, pp. 91–98, Jan. 2018, doi: 10.1109/MMM.2017.2759640.

[19] A. Koelpin, G. Vinci, B. Laemmle, D. Kissinger, and R. Weigel, "The six-port in modern society," IEEE Microw. Mag., vol. 11, no. 7, pp. 35–43, Dec. 2010, doi: 10.1109/MMM.2010.938584.

[20] K. Staszek, S. Linz, F. Lurz, S. Mann, R. Weigel, and A. Koelpin, "Improved calibration procedure for six-port based precise displacement measurements," in Proc. IEEE Topical Conf. Wireless Sensors Sensor Netw. (WiSNet), Jan. 2016, pp. 60–63, doi: 10.1109/WISNET.2016.7444322.

[21] N. K. Mallat and S. O. Tatu, "Six-port receiver in millimeter-wave systems," in Proc. IEEE Int. Conf. Syst., Man Cybern., Oct. 2007, pp. 2693–2697, doi: 10.1109/ICSMC.2007.4414229.

[22] B. Laemmle, K. Schmalz, J. Borngraeber, J. C. Scheytt, R. Weigel, A. Koelpin, and D. Kissinger, "A fully integrated 120-GHz six-port receiver front-end in a 130-nm SiGe BiCMOS technology," in Proc. IEEE 13th Topical Meeting Silicon Monolithic Integr. Circuits RF Syst., Jan. 2013, pp. 129–131, doi: 10.1109/SiRF.2013.6489455.

[23] M. Voelkel, S. Mann, M. Frank, R. Weigel, and A. Hagelauer, "A high precision reconfigureable bistatic interferometric radar with integrated six-port receiver at 60 GHz," in Proc. 12th German Microw. Conf. (GeMiC), Mar. 2019, pp. 48–50, doi: 10.23919/GEMIC.2019.8698190.

[24] M. Voelkel, S. Pechmann, H. J. Ng, D. Kissinger, R. Weigel, and A. Hagelauer, "An integrated bistatic 4TX/4RX six-port MIMO-transceiver at 60 GHz in a 130-nm SiGe BiCMOS technology for radar applications," in IEEE MTT-S Int. Microw. Symp. Dig., Los Angeles, CA, USA, Aug. 2020, pp. 1219–1222, doi: 10.1109/IMS30576.2020.9224001.

[25] B. Zouggari, D. Hammou, C. Hannachi, and S. O. Tatu, "High dynamic range low power drive quadrature millimeter-wave demodulator," in *Proc. 48th Eur. Microw. Conf. (EuMC)*, Sep. 2018, pp. 255–258, doi: 10.23919/EuMC.2018.8541411.

[26] K. Haddadi, D. Glay, and T. Lasri, "Homodyne dual six-port network analyzer and associated calibration technique for millimeter wave measurements," in *Proc. IEEE Int. Symp. Circuits Syst.*, May 2006, p. 4.

[27] K. Haddadi, H. El Aabbaoui, B. Gorisse, D. Glay, N. Rolland, and T. Lasri, "A fully InP monolithic integrated millimeter-wave reflectometer," in *Proc. Eur. Microw. Conf.*, Sep. 2006, pp. 703–706, doi: 10.1109/EUMC.2006.280998.

[28] K. Haddadi, M. M. Wang, K. Nouri, D. Glay, and T. Lasri, "Calibration and performance of two new ultra-wideband four-port-based systems," *IEEE Trans. Microw. Theory Techn.*, vol. 56, no. 12, pp. 3137–3142, Dec. 2008, doi: 10.1109/TMTT.2008.2007138.

[29] K. Haddadi, M. Wang, K. Ziouche, D. Glay, and T. Lasri, "Miniature dual six-port millimeter-wave network analyzer on alumina ceramic substrate," in *Proc. 40th Eur. Microw. Conf.*, Paris, France, Sep. 2010, pp. 1564–1567.

[30] K. Haddadi and T. Lasri, "Formulation for complete and accurate calibration of six-port reflectometer," *IEEE Trans. Microw. Theory Techn.*, vol. 60, no. 3, pp. 574–581, Mar. 2012, doi: 10.1109/TMTT.2011.2181861.

[31] K. Haddadi, M. M. Wang, C. Loyez, D. Glay, and T. Lasri, "Four-port communication receiver with digital IQ-regeneration," *IEEE Microw. Wireless Compon. Lett.*, vol. 20, no. 1, pp. 58–60, Jan. 2010, doi: 10.1109/LMWC.2009.2035969.

[32] K. Haddadi and C. Loyez, "65 nm SOI CMOS 60 GHz passive mixer for six-port technology," in *Proc. IEEE Topical Conf. Wireless Sensors Sensor Netw. (WiSNet)*, Jan. 2016, pp. 52–55, doi: 10.1109/WISNET.2016.7444320.

[33] C. Loyez, M. Bocquet, and K. Haddadi, "Six-port technology for 5G millimeter-wave localization systems," in *Proc. Int. Conf. Electromagn. Adv. Appl. (ICEAA)*, Sep. 2018, pp. 272–275, doi: 10.1109/ICEAA.2018.8520353.

[34] K. Haddadi and T. Lasri, "Six-port technology for millimeter-wave radar and imaging applications," in *Proc. IEEE Topical Conf. Wireless Sensors Sensor Netw. (WiSNet)*, Jan. 2014, pp. 1–3, doi: 10.1109/WiSNet.2014.6825508.

[35] K. Haddadi, M. M. Wang, D. Glay, and T. Lasri, "A 60 GHz six-port distance measurement system with sub-millimeter accuracy," *IEEE Microw. Compon. Lett.*, vol. 19, no. 10, pp. 644–646, Oct. 2009, doi: 10.1109/LMWC.2009.2029744.

[36] K. Haddadi, C. Loyez, L. Clavier, D. Pomorski, and S. Lallemand, "Six-port reflectometer in WR15 metallic waveguide for free-space sensing applications," in *Proc. IEEE Topical Conf. Wireless Sensors Sensor Netw. (WiSNet)*, Jan. 2018, pp. 80–83, doi: 10.1109/WISNET.2018.8311570.

[37] K. Haddadi and T. Lasri, "60-GHz near-field six-port microscope using a scanning slit probe for subsurface sensing," *IEEE Sensors J.*, vol. 12, no. 8, pp. 2575–2576, Aug. 2012, doi: 10.1109/JSEN.2012.2197197.

[38] S. Shopov, N. Cahoon, and S. P. Voinigescu, "Ultra-broadband I/Q RF-DAC transmitters," *IEEE Trans. Microw. Theory Techn.*, vol. 65, no. 12, pp. 5411–5421, Dec. 2017, doi: 10.1109/TMTT.2017.2771457.

[39] J. Pang, S. Maki, S. Kawai, N. Nagashima, Y. Seo, M. Dome, H. Kato, M. Katsuragi, K. Kimura, S. Kondo, and Y. Terashima, "A 50.1-Gb/s 60-GHz CMOS transceiver for IEEE 802.11ay with calibration of LO feedthrough and I/Q imbalance," *IEEE J. Solid-State Circuits*, vol. 54, no. 5, pp. 1375–1390, May 2019, doi: 10.1109/JSSC.2018.2886338.

[40] H. Al-Rubaye and G. M. Rebeiz, "A DC-60 GHz I/Q modulator in 45 nm SOI CMOS for ultra-wideband 5G radios," in *Proc. IEEE BiCMOS Compound Semiconductor Integr. Circuits Technol. Symp. (BCICTS)*, Oct. 2018, pp. 275–278, doi: 10.1109/BCICTS.2018.8551144.

[41] G. Lee, H. Koh, U.-S. Suh, and T. W. Kim, "An IR-UWB angle-of-arrival sensor IC using auto-toggled time-to-digital converter," *IEEE Microw. Wireless Compon. Lett.*, vol. 29, no. 11, pp. 749–752, Nov. 2019, doi: 10.1109/LMWC.2019.2943811.

[42] P. Indirayanti, T. Ayhan, M. Verhelst, W. Dehaene, and P. Reynaert, "A mm-precise 60 GHz transmitter in 40 nm CMOS for discrete-carrier indoor localization," *IEEE J. Solid-State Circuits*, vol. 50, no. 7, pp. 1604–1617, Jul. 2015, doi: 10.1109/JSSC.2015.2414433.

CHRISTOPHE LOYEZ (Member, IEEE) is currently the CNRS Research Director of the Institute of Electronics, Microelectronics and Nanotechnology (IEMN). He has initiated several multidisciplinary research activities on high-speed wireless systems and low-power systems for radiocommunication and localization. He is regularly the scientist in charge of projects on millimeter wave systems and integrated RF systems. He has been accredited to direct research (HDR), since 2012. He is a Thesis Supervisor on energy efficiency systems. Since 2015, he has been the Leader of the Circuits and Systems for Applications of Microwaves (CSAM) Research Group, composed of more than ten researchers, whose research activities concern the energy efficiency of transmission and information processing systems. He is the Co-Leader of the Joint-Laboratory e-COST "Enhanced Communication devices for Smart cities and Transports," which brings together more than 20 researchers from IEMN and Gustave Eiffel University on topics related to smart cities and transport. He is a member of the Organizing Committee of the French Chapter of the IEEE Solid State Circuit.

MICHAEL BOCQUET received the Ph.D. degree in electronics engineering and telecommunications from the University of Sciences and Technologies, Lille, France, in 2007. He worked at INRETS (now Gustave Eiffel University) as a Radio Engineer, in 2008. In 2009, he joined the Institute of Electronic Microelectronic and Nanotechnology (IEMN-DOAE), Université Polytechnique Hauts-de-France, where he is currently an Assistant Professor. His main research interests include RF transceivers for telecommunications, localization systems operating in millimeter-wave frequency bands, and wireless sensor networks. In this domain, he studied networks of wireless sensors for the non-destructive test (NDT) of rails and for the energy efficiency inside railway vehicle.

KAMEL HADDADI (Member, IEEE) received the M.Sc. and Ph.D. degrees from the University of Lille, Villeneuve-d'Ascq, France, in 2003 and 2007, respectively. He is currently an Associate Professor with the Institute of Electronics, Microelectronics and Nanotechnology, joint research unit between the University of Lille and the CNRS. He is the Head of the Lab-Space RF-2S (Radio-Frequency Sensing and Services) dedicated to the development of microwave/mm-wave instrumentation and sensors for nondestructive testing applications. The results achieved in this context led to publication of around 100 articles in peer-review international papers and conferences. He is a member of the International Committees: IEEE MTT-8 RF Nanotechnology and IEEE MTT-24 Microwave/mm-Wave Radar, Sensing and Array Systems, and a TPC member in various IEEE conferences. He is an Associate Editor of IEEE TRANSACTIONS ON INSTRUMENTATION AND MEASUREMENT.

• • •